

Numerical Heat Transfer, Part A: Applications



Date: 05 July 2017, At: 07:21

An International Journal of Computation and Methodology

ISSN: 1040-7782 (Print) 1521-0634 (Online) Journal homepage: http://www.tandfonline.com/loi/unht20

Double Diffusive Natural Convection in a Porous Rhombic Annulus

F. Moukalled & M. Darwish

To cite this article: F. Moukalled & M. Darwish (2013) Double Diffusive Natural Convection in a Porous Rhombic Annulus, Numerical Heat Transfer, Part A: Applications, 64:5, 378-399, DOI: 10.1080/10407782.2013.784656

To link to this article: http://dx.doi.org/10.1080/10407782.2013.784656

	Published online: 22 May 2013.
	Submit your article to this journal ${\it \mathbb{G}}$
ılıl	Article views: 98
a`	View related articles 🗗
2	Citing articles: 10 View citing articles 🗹

Full Terms & Conditions of access and use can be found at http://www.tandfonline.com/action/journalInformation?journalCode=unht20

Numerical Heat Transfer, Part A, 64: 378-399, 2013

Copyright © Taylor & Francis Group, LLC ISSN: 1040-7782 print/1521-0634 online DOI: 10.1080/10407782.2013.784656



DOUBLE DIFFUSIVE NATURAL CONVECTION IN A POROUS RHOMBIC ANNULUS

F. Moukalled and M. Darwish

Department of Mechanical Engineering, American University of Beirut, Beirut, Lebanon

This article reports on an investigation performed to study laminar steady state double diffusive natural convection in a two-dimensional porous enclosure of rhombic cross-section. Solutions are obtained numerically using a finite volume method for the case when the inner wall is uniformly heated to a temperature T_h while subjected to a high solute concentration Sh, and the outer wall is evenly cooled to a temperature Tc while exposed to a low solute concentration S_c. Simulations are conducted for several values of Rayleigh number (Ra), Darcy number (Da), Prandtl number (Pr), porosity (ε), and enclosure gap (E_{e}) for fixed values of Lewis number (Le = 10) and buoyancy ratio (N = 10). The results are displayed in terms of streamlines, isotherms, isoconcentrations, mid-height velocity, temperature, concentration profiles, and local and average Nusselt and Sherwood number values. Predictions indicate that for the Lewis number and buoyancy ratio considered, the flow field is more affected by mass transfer than by heat transfer. Moreover, convection effects increase with an increase in Ra, Da, E₂, and/or ε. The porosity of the porous matrix has no effect on the flow, temperature, and concentration fields at low values of Darcy number. Furthermore, the total heat and mass transfer increases as Pr increases and/or as the enclosure gap decreases due to an increase in the wall area over which heat and mass transfer occur. Values of \overline{Nu} and \overline{Sh} indicate dominant diffusion at low Ra number values with convection affecting the total heat and mass transfer at high Ra values.

INTRODUCTION

Double diffusive natural convection flows in porous media resulting from the combined buoyancy effects of concentration and temperature gradients arise in a variety of industrial applications such as migration of moisture in fibrous insulation, the growth of crystals, food processing, solar energy systems, etc. [1–4]. While a number of studies in simple porous rectangular enclosures appear in the literature [5–8], only a few investigations in complex geometries have been reported [9–12]. The focus of the present investigation is to analyze the effects of porosity on double diffusive natural convection in a porous annulus between two horizontal pipes of rhombic cross section.

Received 8 December 2012; accepted 12 February 2013.

The financial support provided by the University Research Board of the American University of Beirut is gratefully acknowledged.

Address correspondence to F. Moukalled, Department of Mechanical Engineering, America University of Beirut, P. O. Box 11 0236, Riad El Solh, Beirut 1107 2020, Lebanon. E-mail: memouk@aub.edu.lb

	NOMENCLATURE									
A	wall area	T	dimensional temperature							
$ \begin{array}{c} A \\ c_p \\ d_p \\ D \\ D_o \\ Da \\ E_g \\ F \\ \mathbf{g} \\ h \\ \bar{h} \end{array} $	specific heat pores diameter mass diffusion coefficient length of pipe's main diagonal Darcy number enclosure gap ratio constant in Forchheimer's extension gravitational acceleration local convection heat transfer coefficient average convection heat transfer	u, U v, V v, V x, y X, Y α β μ	dimensional and dimensionless x-velocity component dimensional and dimensionless y-velocity component dimensional and dimensionless velocity vector dimensional coordinates dimensionless coordinates thermal diffusivity expansion coefficient dynamic viscosity							
k	coefficient fluid thermal conductivity permeability of the porous media Lewis number unit vector normal to surface buoyancy ratio	ρ ε Ω ψ σ	density dimensionless temperature porosity rhombus angle stream function dimensionless solute concentration							
Nu P P Pr Ra S Sh Sh	local Nusselt number average Nusselt number dimensional pressure dimensionless pressure Prandtl number Rayleigh number dimensional solute concentration local Sherwood number average Sherwood number	Subscri c h i m o s T	cold wall or convection heat transfer hot wall condition at inner pipe mass transfer condition at outer pipe refers to concentration refers to temperature							

Several workers reported on double diffusive natural convection in square and rectangular enclosures. Lee et al. [13] analyzed numerically, using the finitedifference method, natural convection in a square enclosure filled with a salt water solution and laterally heated along its side. Four distinct flow regimes were observed depending on the magnitude of solutal stratification relative to thermal buoyancy. Lee and Hyun [14] conducted a numerical study of double diffusive convection in a rectangular cavity with combined horizontal temperature and concentration gradients such that the thermal and solutal buoyancy effects are counteracting, resulting in an opposing gradient flow configuration. Borjini et al. [15, 16] studied numerically the two-dimensional hydromagnetic double diffusive convection of a radiatively participating fluid confined in a rectangular enclosure. In the work reported in [15], Borjini et al. imposed uniform temperatures and concentrations along the vertical walls, while assuming the horizontal walls to be adiabatic and impermeable. In reference [16] however, Borijini et al. analyzed the mechanisms of the transitions between steady compositionally dominated flow and unsteady thermally dominated flow for fixed Prandtl, Rayleigh, and Lewis numbers. Han and Kuehn [17] analyzed numerically double diffusive natural convection in a vertical rectangular cavity of aspect ratio 4. Double diffusive multicell flow structures observed in experiments by the authors were simulated successfully. Wang et al. [18] studied experimentally, using particle image velocimetry (PIV), double diffusive convection of a binary NH₄Cl-H₂O solution in a rectangular enclosure during solidification. The double diffusive flow was found to be strong at the beginning of solidification and decayed as solidification proceeded.

Investigators have also reported on double diffusive natural convection heat transfer in non-rectangular enclosures. Hi and Lu [19] simulated, using a finite element method, transient double diffusive convection in a vertical cylinder to identify the effect of the buoyancy ratio on the evolution of the flow, temperature, and solute fields. Lee et al. [20] conducted an experimental investigation to study the double diffusive convection phenomena of a stably-stratified salt-water solution due to lateral heating in a stationary and rotating annulus. Dosch and Beer [21] studied numerically and experimentally unsteady double diffusive convection in a horizontal concentric annulus filled with an H₂O-NaCl solution. Reported results indicated a considerable decrease in heat transfer as compared to natural convection without a stabilizing salt gradient. Liou and Hong [22] investigated double diffusive natural convection in a V-shaped sump using a control volume method for two types of boundary conditions involving temperature and concentration distributions. Kumar et al. [23] examined, using a velocity-vorticity formulation, convection driven by combined thermal and solutal concentration buoyancy effects in a lid-driven square cavity under aiding and opposing temperature and concentration gradients along the vertical direction. Kumar et al. [24] extended the analysis in reference [23] to include a heated block in the cavity.

Suárez et al. [25] evaluated the effects of double diffusive convection on the thermal performance and stability of a salt-gradient solar pond and showed that neglecting the effect of double diffusive convection over-estimate the temperatures at the bottom of the pond. Kranenborg and Dijkstra [26] performed direct numerical simulation of convective flows in both salt-stratified and non-stratified liquids generated by a cooled slab of solid material. Results revealed flows of double diffusive origin when the background liquid is stratified through a constant salt gradient. Dijkstra and Kranenborg [27] studied the formation of double diffusive layer in a laterally heated liquid which is stably stratified through a constant vertical salinity gradient. Tanny and Gotlib [28] reported a numerical study, using the Galerkin method, of an infinite horizontal double diffusive layer stratified vertically by temperature and solute concentration for the case of temperature-dependent viscosity and salt diffusivity. Kranenborg and Dijkstra [29] investigated through direct numerical simulation the nonlinear evolution of double diffusive instabilities into a laterally heated stably stratified motionless liquid.

Several investigations were also conducted in the turbulent flow regime. Van Der Eyden et al. [30] presented numerical and experimental results of turbulent double diffusive natural convection of a mixture of two gases in a trapezoidal enclosure. Numerically generated results were in satisfactory agreement with measurements. Hullender and Laster [31] used a low Reynolds number k- ϵ model to predict the wind-induced entrainment in a double diffusive system. Good agreement with experimental data was obtained for wind speeds less than $10\,\text{m/s}$. De Lemos and Tofaneli [32] investigated turbulent double diffusive natural convection and analyzed the stability of mixtures under gradients of temperature and concentration.

A number of studies on double diffusive natural convection in porous enclosures have also appeared in the literature. Karimi-Fard et al. [33] studied numerically, using the finite volume method, the effect of Darcy and Lewis number on double

diffusive natural convection in a square cavity filled with a porous medium. Their study revealed that the inertial and boundary effects have a profound influence on the double diffusive convection. Chamkha [34] reported on unsteady, laminar double diffusive convective flow of a binary gas mixture in a rectangular enclosure filled with a uniform porous medium subject to a temperature-dependent heat source or sink. Bennacer et al. [35] presented a study on double diffusive natural convection in a square cavity filled with porous media heated and cooled along vertical walls by uniform heat fluxes when a solutal flux is imposed vertically. Beji et al. [36] carried out a numerical investigation to study the combined effects of thermal and solutal buoyancy forces on the flow, heat, and mass transfer in a vertical annular porous layer subjected to constant temperature and concentration boundary conditions. Costa [37, 38] predicted numerically double diffusive natural convection in parallelogrammic enclosures filled with fluid-saturated porous media. Results showed the strong potential of this configuration for heat and mass transfer applications. Kumar et al. [39] conducted a numerical study, using the Galerkin finite element method, on combined heat and mass transfer by natural convection in a porous enclosure. Saghir and Islam [40] performed a numerical study, using a finite element formulation for a wide range of permeability contrasts, of double diffusive phenomena in porous media.

Natural convection heat transfer in a porous annulus of rhombic cross-section was recently investigated by Moukalled and Darwish [12]. The intention of this article is to extend the work reported in reference [12], and to study double diffusive natural convection heat transfer in the same geometry for the case when the porous enclosure is filled with a salty fluid.

PHYSICAL MODEL AND GOVERNING EQUATIONS

The physical domain is displayed in Figure 1a, and represents the annulus between two concentric horizontal pipes of rhombic cross-sections. The length of the main diagonal of the inner and outer pipe is D_i and D_o , respectively. The walls of the inner pipe are maintained at high temperature and solute concentration (T_h and S_h), while the walls of the outer pipe are kept at low temperature and solute concentration (T_c and S_c). Because of symmetry, computations are performed only on the right half of the enclosure, which is assumed to be filled with a porous material of porosity ε . The differences in temperature and concentration between the inner and outer walls create density variations within the fluid filling the porous enclosure and give rise to the buoyancy forces that move the flow, which is assumed to be steady, incompressible, and two-dimensional. Moreover, the convective fluid and the porous matrix are assumed to be everywhere in local thermodynamic equilibrium. The non-Darcian Forchheimer's [41] and Brinkman's [42] extensions are included in the conservation equations to better model the physical situation. With these assumptions, and employing the Boussinesq approximation with the thermo physical properties of the working fluid assumed to be constant, except for density variations in the body force term, the volume-averaged equations [43] governing conservation of mass, momentum, energy, and solute are, respectively, written as follows.

$$\nabla \cdot \mathbf{v} = 0 \tag{1}$$

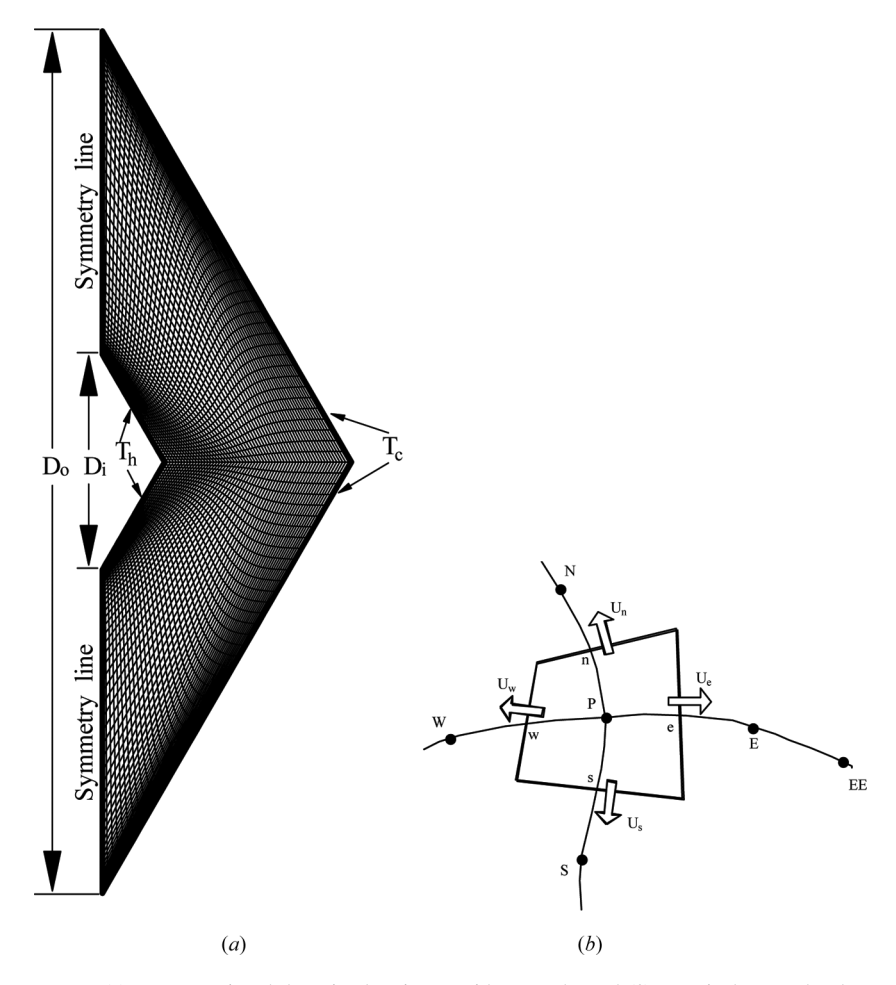


Figure 1. (a) Computational domain showing a grid network, and (b) a typical control volume.

$$\begin{split} &\frac{\rho}{\varepsilon^2}(\mathbf{v}\cdot\nabla)\mathbf{v} = \frac{\mu}{\varepsilon}\nabla^2\mathbf{v} - \nabla p - \frac{\mu}{K}\mathbf{v} \\ &- \frac{F}{K^{1/2}}\rho|\mathbf{v}|\mathbf{v} - \rho[\beta_t(T-T_\infty) + \beta_s(S-S_\infty)]\mathbf{g} \end{split} \tag{2}$$

$$\varepsilon(\rho c_p)\mathbf{v}\cdot\nabla T = \nabla\cdot(k\nabla T) \tag{3}$$

$$\mathbf{v} \cdot \nabla S = \nabla \cdot (D \nabla S) \tag{4}$$

Defining the dimensionless variables as,

$$X = \frac{x}{D_o}, \ Y = \frac{y}{D_o}, \ U = \frac{u}{\sqrt{g\beta_t(T_h - T_c)D_o}}, \ V = \frac{v}{\sqrt{g\beta_t(T_h - T_c)D_o}}$$
 (5a)

$$P = \frac{p + \rho g y}{\rho g \beta_t (T_h - T_c) D_o}, \theta = \frac{T - T_c}{T_h - T_c}, Ra_t = \frac{\rho g \beta_t \Delta T D_o^3}{\mu \alpha}, Pr = \frac{\mu c_p}{k}, \sigma = \frac{S - S_c}{S_h - S_c}$$
(5b)

$$Ra_{s} = \frac{\rho g \beta_{s} \Delta S D_{o}^{3}}{\mu \alpha}, Le = \frac{\alpha}{D}, Da = \frac{K}{D_{o}^{2}}, F = \frac{1.75}{\sqrt{150\epsilon^{3}}}, K = \frac{\epsilon^{3} d_{p}^{2}}{150(1-\epsilon)^{2}}$$
(5c)

the nondimensional form of the conservation equations becomes the following.

$$\Delta \cdot \mathbf{V} = 0 \tag{6}$$

$$\frac{1}{\varepsilon^2}(\mathbf{V}\cdot\nabla)\mathbf{V} = \frac{1}{\varepsilon}\sqrt{\frac{Pr}{Ra_t}}\nabla^2\mathbf{V} - \nabla P - \frac{1}{Da}\sqrt{\frac{Pr}{Ra_t}}\mathbf{V} - \frac{F}{\sqrt{Da}}|\mathbf{V}|\mathbf{V} + \left(\theta + \frac{Ra_s}{Ra_t}\sigma\right)\mathbf{j} \quad (7)$$

$$\mathbf{V} \cdot \nabla \theta = \frac{1}{\sqrt{Ra_t Pr}} \nabla^2 \theta \tag{8}$$

$$\mathbf{V} \cdot \nabla \sigma = \frac{1}{\text{Le}\sqrt{\text{Ra}_{l}\text{Pr}}} \nabla^{2} \sigma \tag{9}$$

The meaning of the various dimensionless numbers is given in the nomenclature. The boundary conditions used are as follows.

$$U = \frac{\partial V}{\partial X} = \frac{\partial \theta}{\partial X} = \frac{\partial \sigma}{\partial X} = 0 \qquad \text{along symmetry lines}$$
 (10)

$$U = V = 0, \theta = \sigma = 1$$
 at inner walls (11)

$$U = V = \theta = \sigma = 0$$
 at outer walls (12)

SOLUTION PROCEDURE

The buoyancy term appearing in the y-momentum equation (Eq. (7)) couples the hydrodynamic field (Eqs. (6) and (7)) to the thermal (Eq. (8)) and mass transfer (Eq. (9)) fields and necessitates a simultaneous solution of all equations. In this work, these equations are solved numerically using the finite volume method. Solutions are obtained by subdividing the physical domain, depicted in Figure 1a, into a number of control volumes each associated with a grid point placed at its geometric center (Figure 1b). In every control volume, the partial differential equations (Eqs. (6)–(9)] are integrated and transformed into algebraic equations through profile approximations for the diffusion [44] and convection (the SMART scheme [45], applied within the context of the NVSF methodology [46], is used here) terms. The integral value of the source term over a control volume (Figure 1b) is evaluated by assuming the source at the control volume center to be equal to the mean value over the whole control volume. The collection of these algebraic equations over the entire domain forms a system that is iteratively solved. To evaluate the pressure field, a pressure correction is defined and a pressure correction equation is derived

by combining the momentum and continuity equations as in the SIMPLE procedure of Patankar [47–49]. A collocated grid is used in the present study, and checkerboard pressure and velocity fields are suppressed through the use of the momentum weighted interpolation method (MWIM), while calculating the mass fluxes across the control volume faces [50].

Numerical Accuracy and Validation

The accuracy and grid independence of the results are established by comparing solutions obtained over a number of grid systems. A final grid with a size of (160×128) control volumes is used to generate all results presented here. The grid points are nonuniformly distributed over the domain and symmetry lines where higher gradients are expected (Figure 1a). The comparison of solutions for some of the cases with similar ones obtained on a denser grid with a size of (240×240) control volumes revealed that the maximum differences in the average Nusselt and Sherwood number values were less than 0.0156%. Conservation of the various physical quantities was satisfied to within 10^{-8} for each control volume.

The correctness of the solution procedure is verified by comparing results obtained from the present model with corresponding results reported in the literature for double diffusive natural convection in a square [33] and a parallelogrammic [37] porous enclosure. For the square enclosure, computed average Nusselt and Sherwood number values (N = 0, Le = 10, and Ra = 100 and 200) are compared in Table 1 with values reported by several workers [33, 51, 52] and is seen to be in good agreement. For the parallelogrammic enclosure problem, the computed average Nusselt and Sherwood number values (for N=2, Le=0.8, and R $a_t=25$) are compared in Figures 2a and 2b, respectively, with similar ones reported by Costa [37]. In the calculations, the same nonuniform grid with an expansion ratio of 1.05 and of size (101×101) grid points suggested in reference [37] is used. The problem is solved for an enclosure with an aspect ratio H/L = 0.5 and for an inclination angle (θ) values varying between -60° and 60° with a step size of 10° . An initial comparison was done between values reported by Costa [37] using the ψ formulation and results generated using the full model formulation with the SIMPLE algorithm. Whereas Nu values were in good agreement, reported Sh values were much higher than the calculated ones. A review of the code did not reveal any error. To get more insight into these differences, the problem was solved via the ψ formulation using the

Table 1. Comparison of current average Nusselt and Sherwood number results in a square enclosure (Le=10, N=0), with similar ones reported by Karimi-Fard et al. [33], Goyeau et al. [51], and Trevisan and Bejan [52]

		Ra = 1	00		Ra = 200					
	Present work	Ref. [33]	Ref. [51]	Ref. [52]	Present work	Ref. [33]	Ref. [51]	Ref. [52]		
Nu Sh	3.104 13.379	3.11 13.43	3.11 13.25	3.27 15.61	4.954 20.182	4.97 20.32	4.96 19.86	5.61 23.23		

same developed code, which is a general one. For that purpose, slight modifications were required. As depicted in Figure 2, results were very close to the ones generated using the SIMPLE approach. To further confirm the correctness of results, an

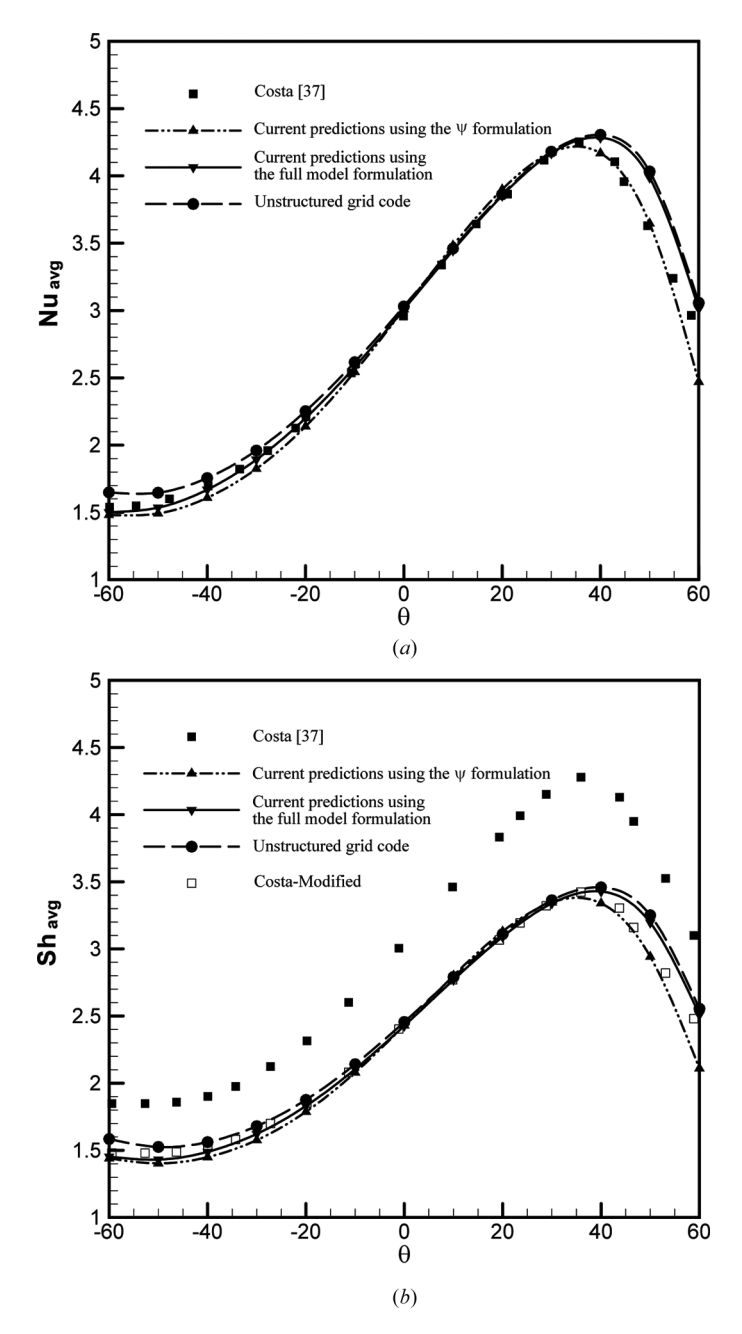


Figure 2. Comparison of predicted average (a) Nusselt and (b) Sherwood numbers in a parallelogrammic enclosure with similar ones reported by Costa [37].

unstructured grid code was employed to solve the problem. Again, \overline{Sh} values were lower than the values reported by Costa [37] and very close to those generated with the code used to obtain results reported here. The interesting observation was that Nu values reported by Costa and generated in this work were very close. This fact has led the authors to compare the energy and concentration equations used by Costa [37]. The difference turned out to be in the diffusion coefficient, which is equal to 1 for temperature, but 1/Le for the solute. It became clear that fluxes used by Costa [37] to calculate $\overline{\text{Nu}}$ and $\overline{\text{Sh}}$ were directly taken from their code, which are multiplied by the diffusion coefficients. For the case of the Nusselt number, because the diffusion coefficient of the dimensionless energy equation is 1, it did not result in any difference. However, for the Sherwood number the diffusion coefficient of the concentration equation is 1/Le (Le = 0.8) and it resulted in higher values. By dividing the \overline{Sh} values reported in reference [37] by the diffusion coefficient, the variation in the Sherwood number values with θ fell on top of the ones generated in this work (Figure 2a), confirming the correctness of the developed solution procedure. Therefore, the Sherwood number values reported in reference [37] are actually \overline{Sh}/Le .

RESULTS AND DISCUSSION

The geometric parameters affecting the hydrodynamic, heat transfer, and mass transfer fields are the rhombus angle, which is fixed at 30°, and the enclosure gap $(E_g = 1 - D_i/D_o)$, which is assigned three different values $(E_g = 0.875, 0.75, \text{ and } 0.5)$. On the other hand, the thermophysical parameters in the problem are: the porosity (ϵ), the Rayleigh number (Ra), the Prandtl number (Pr), the Darcy number (Da), the buoyancy ratio $(N = \text{Ra}_s/\text{Ra}_t)$, and the Lewis number (Le). Air and water are considered to be the working fluids and, as such, the Prandtl number is assigned the two values of 0.7 and 5 while the Lewis number and buoyancy ratio are fixed at 10. Moreover, three different values of Rayleigh number (Ra = 10^5 , 10^6 , and 10^7), two different values of Darcy number (Da = 10^{-3} , and 10^{-5}), and three different values of porosity ($\epsilon = 0.3$, 0.6, and 0.9) are considered.

Results are presented in the form of streamlines, isotherms, isoconcentrations, mid-height velocity, temperature, and concentration profiles, and local and average Nusselt and Sherwood number values.

Streamlines, Isotherms, and Isoconcentrations

The influence of the various parameters on the flow, temperature, and concentration fields is revealed by the streamline, isotherm, and isoconcentration plots depicted in Figures 3–6. Figures 3 and 5 present results for a Rayleigh number with a value of 10^5 , while Figures 4 and 6 are for Ra = 10^7 . Moreover, results for the highest enclosure gap ($E_g = 0.875$) are presented in Figures 3 and 4, while contours in the lowest enclosure gap ($E_g = 0.5$) are shown in Figures 5 and 6. Contours are plotted for two values of Darcy number (Da = 10^{-5} and 10^{-3}), for three values of porosity ($\varepsilon = 0.3$, 0.6, and 0.9), and for Pr = 0.7. In all figures, streamlines are displayed in plots (a)–(c) and (b)–(m), isotherms in plots (d)–(f) and (n)–(g), and isoconcentrations in plots (g)–(i) and (g)–(i).

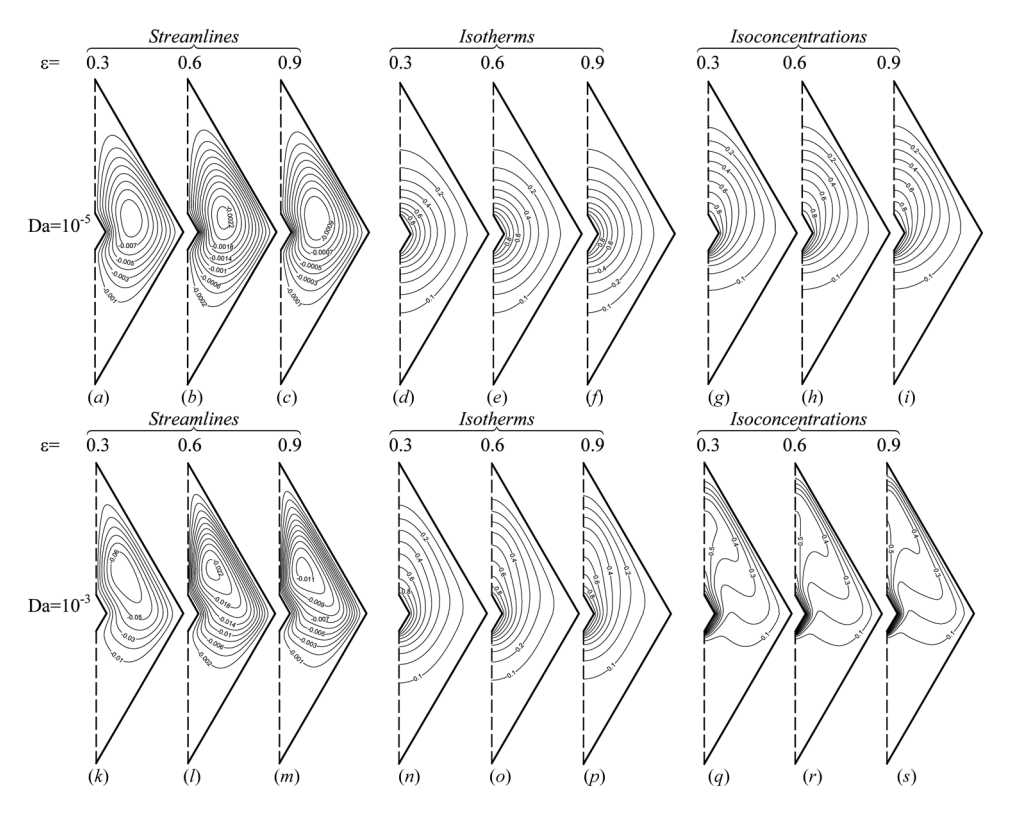


Figure 3. (a)–(c), (k)–(m) Streamlines (d)–(f), (n)–(p) isotherms, and (g)–(i), (q)–(s) isoconcentrations for different values of ε and Da ($E_g = 0.875$, N = 10, Le = 10, Pr = 0.7, and Ra = 10^5).

In this work, the stream function is defined as follows,

$$\frac{1}{\varepsilon^2}U = \frac{\partial \psi}{\partial Y} \text{ and } \frac{1}{\varepsilon^2}V = -\frac{\partial \psi}{\partial X}$$
 (13)

and is calculated by integrating numerically the above equation.

At the lowest values of Ra_t and Da and the highest value of E_g (Figure 3), the flow is weak and for $\varepsilon = 0.3$ streamlines are almost symmetrical with respect to the horizontal centerline of the domain (Figure 3a). As porosity increases, the flow asymmetry increases with the center of the recirculating eddy characterizing the flow, moving slightly upward to the upper half of the domain (Figures 3b and 3c). This behavior is more visible at higher Da value (Figures 3k-3m), where the flow is much stronger and the eye of the recirculating eddy is almost in the middle of the upper half of the domain. The increase in the strength of the flow with Da is due to an increase in the permeability of the porous medium $(Da = K/D_o^2)$. The effect of porosity on K can be inferred from its functional relationship (Eq. (5)), which can be rewritten as follows.

$$K = \frac{\varepsilon^3 d_p^2}{150(1-\varepsilon)^2} = \frac{d_p^2}{150} \varepsilon^3 (1 + \varepsilon + \varepsilon^2 + \dots)^2$$
 (14)

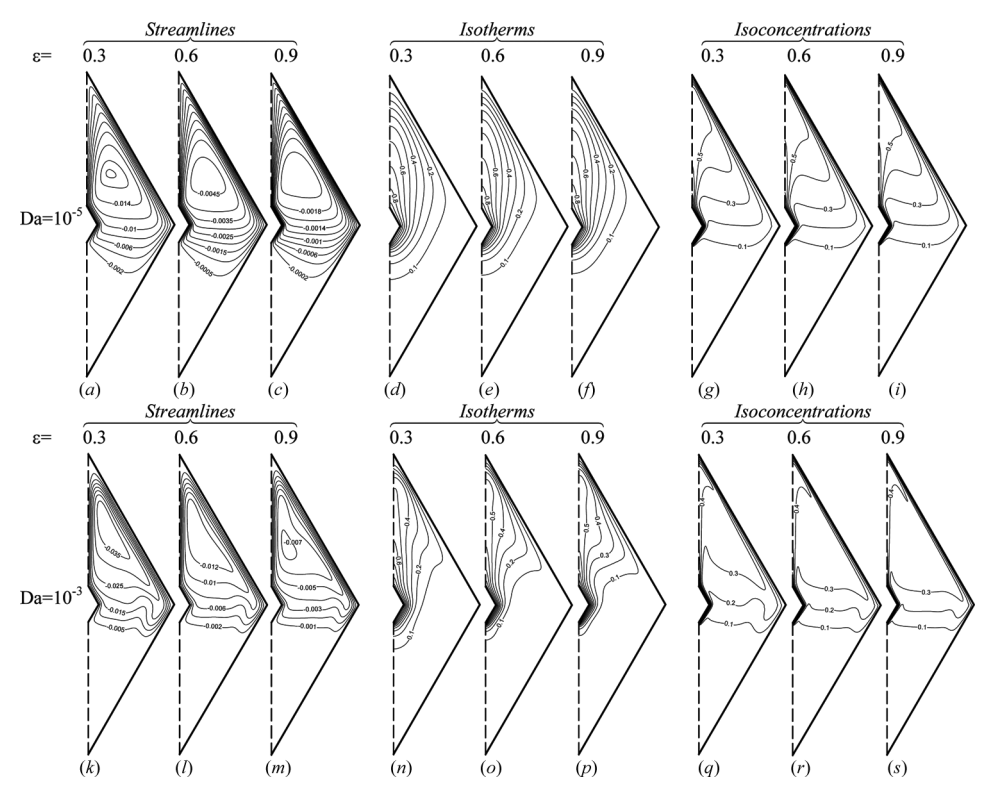


Figure 4. (a)–(c), (k)–(m) Streamlines (d)–(f), (n)–(p) isotherms, and (g)–(i), (q)–(s) isoconcentrations for different values of ε and Da ($E_g = 0.875$, N = 10, Le = 10, Pr = 0.7, and Ra = 10^7).

From Eq. (14), it is clear that an increase in ϵ at constant Da implies a decrease in the diameter of the porous matrix. This decrease is associated with an increase in the surface area and, consequently, friction losses and a decrease in pressure drop. These counteracting effects compete to determine the flow field. Results clearly indicate an increase in the flow strength as ϵ increases, which indicate that the decrease in the form drag is higher than the increase in friction drag. Because of these two opposing effects, the flow strength is more affected by Da than by ϵ . The decrease in the values of ψ as the flow strength increases (at higher ϵ) is due to the way the streamfunction values are calculated [equation (13)].

The symmetrical distribution of isotherms at low Da presented in Figures 3d–3f reflects the above described behavior with the distribution of isotherms becoming asymmetrical at higher Da values (Figures 3n–3p). Nevertheless, effects of convection due to temperature gradient are low at this value of Ra_t as reflected by the slight distortion of the isotherms with thermal stratification confined to a small region in the lower part of the rhombic annulus. Temperature-driven convection effects are seen to slightly increase with increasing values of porosity, which is more visible at $Da = 10^{-3}$.

Isoconcentration maps displayed in Figures 3g-3i and 3q-3s indicate stronger concentration-driven buoyancy effects especially at high Da (Figures 3q-3s). This is expected as Ra_s is an order of magnitude higher than Ra_t (i.e., N=10), and is

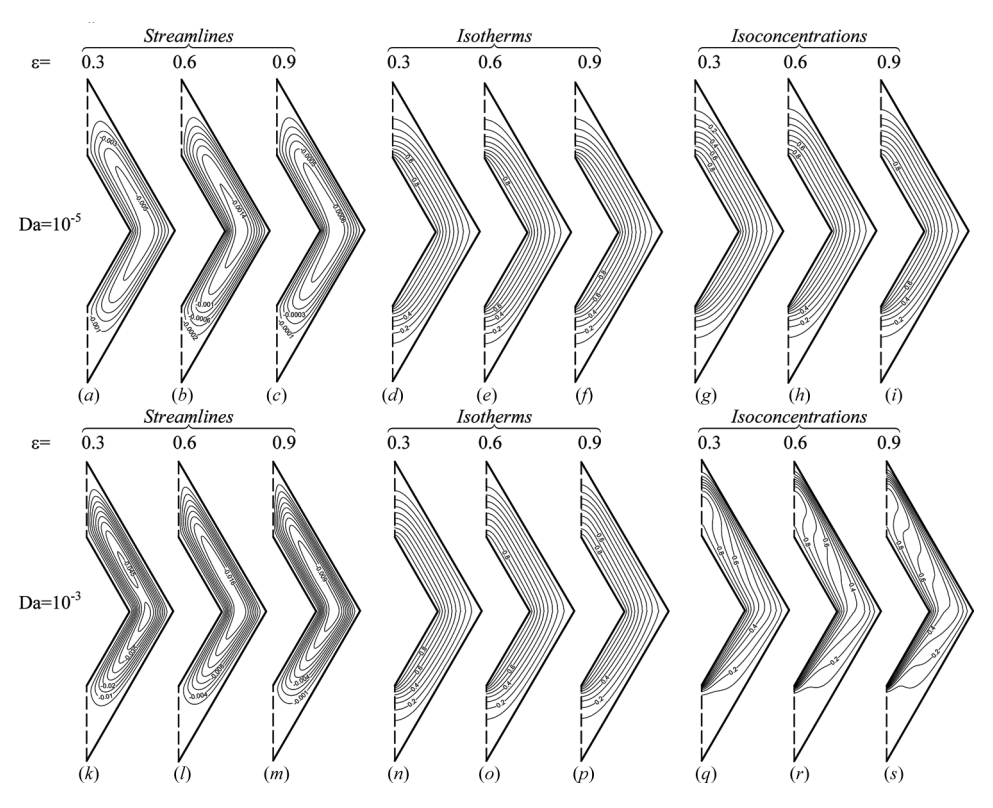


Figure 5. (a)–(c), (k)–(m) Streamlines (d)–(f), (n)–(p) isotherms, and (g)–(i), (q)–(s) isoconcentrations for different values of ε and Da ($E_g = 0.5$, N = 10, Le = 10, Pr = 0.7, and Ra = 10^5).

reflected by the higher stratified concentration region in the lower part of the domain and the higher asymmetry and distortion in isoconcentration lines. This behavior is due to the significantly larger area of the surface with low solute concentration relative to the area of the surface with high solute concentration. Below the horizontal diagonal the surface with low solute concentration promotes stratification in the lower half, and above the diagonal the surface with high solute concentration promotes stratification in the upper half. Since the lower half is dominated by the much larger surface area with low concentration, there is significant stratification in the lower half, as seen in Figures 3q-3s. Because of the high level of stratification in the lower half, the flow cannot easily penetrate the lower region, and as seen in Figures 3k-3m, the flow in this region is essentially very weak. In the upper half, due to the relatively lower proportion of surface area with high solute concentration, stratification is not significant, and a strong recirculating flow is obtained. Again concentration-driven convection is seen to increase with increasing ε as reflected by the denser clustering of isoconcentration lines near the walls of the enclosure.

At higher Ra_t values (Figure 4), the flow is stronger with the eye of the recirculating eddy moving further upward. This is due to the increase in the buoyancy forces, which are directly proportional to Ra_t . Isotherms (Figures 4d-4f and 4n-4p) and isoconcentrations (Figures 4g-4i and 4q-4s) show the boundary layer behavior

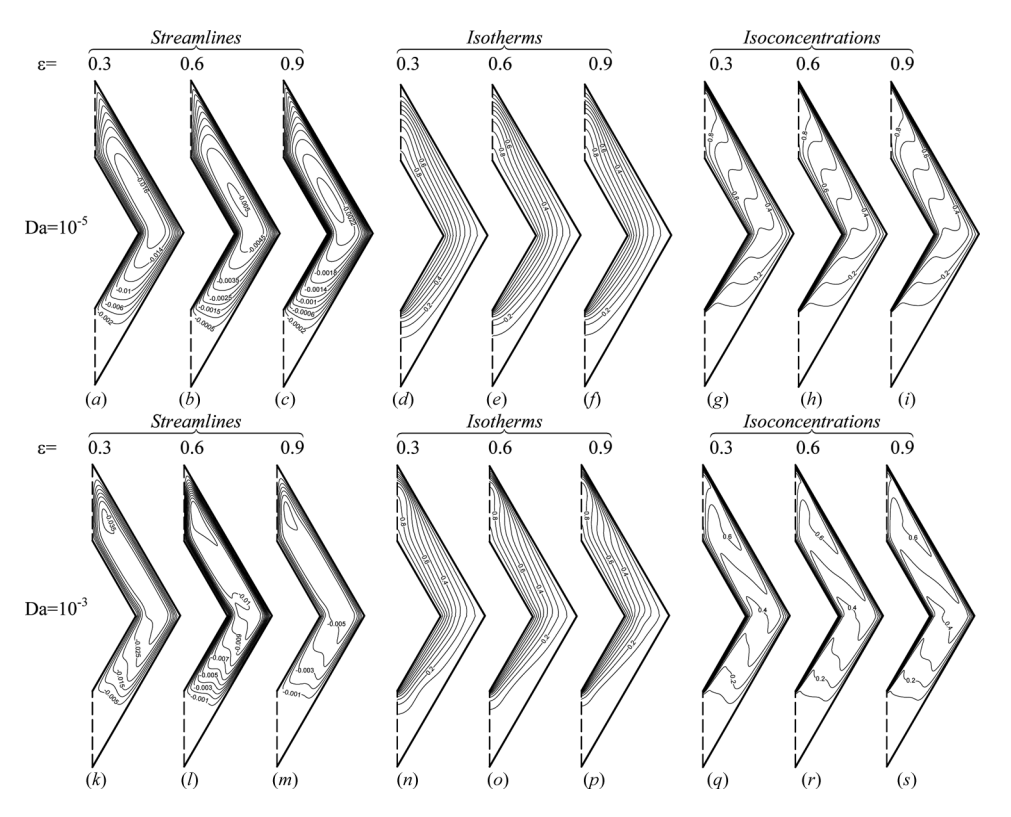


Figure 6. (a)–(c), (k)–(m) Streamlines (d)–(f), (n)–(p) isotherms, and (g)–(i), (q)–(s) isoconcentrations for different values of ε and Da ($E_g = 0.5$, N = 10, Le = 10, Pr = 0.7, and Ra = 10^7).

on the lower part of the heated surface and the upper part of the cooled enclosure surface. The boundary layer along the inner wall rises up from the upper region of the inner body and forms a thermal plume. This can be seen as isotherms and isoconcentrations move away from the inner wall near the top. Again the flow strength increases with increasing ϵ and/or Da values (Figures 4a-4c and 4k-4m). Higher stratification levels are obtained in comparison with levels at lower values of Ra, with the flow being more affected by concentration gradients than temperature gradients (N=10). This is evident from isotherms presented in Figures 4d-4f and 4n-4p and isoconcentrations depicted in Figures 4g-4i and 4q-4s). The distribution of isotherms and isoconcentrations is asymmetric even at low Da value. A large thermally stratified region forms in the lower part of the domain with heat transfer in the non-stratified region occurring, at low Da, mainly by conduction. This can be inferred from Eqs. (8) and (9), where the convection term in the solute conservation equation is multiplied by the Lewis number (Le = 10) indicating that the concentration distribution is more affected by convection than the temperature distribution. At high Da, the thermally stratified region is larger and convection is stronger as reflected by the higher distortion of isotherms.

As the enclosure gap decreases [$E_g = 0.5$, Figures 5 and 6], the proportion of the hot/high solute to the cold/low solute surface increases (approaching unity),

the stratification effects in the lower half of the enclosure become less noticeable and at low Ra_t and Da the flow patterns in the upper and lower halves are similar (Figures 5a-5c). The decrease in the strength of the flow with increasing values of the enclosure gap is due to a decrease in the available convective area and to the greater viscous effects of the added surface area.

Velocity, Temperature, and Concentration Profiles

Figure 7 shows horizontal velocity, vertical velocity, temperature, and concentration profiles along the horizontal centerline of the cavity plotted in terms of a dimensionless distance $(\Delta X/\Delta X_{max})$ defined as follows.

$$\frac{\Delta X}{\Delta X_{max}} = \frac{X - X_{min}}{X_{max} - X_{min}} \tag{15}$$

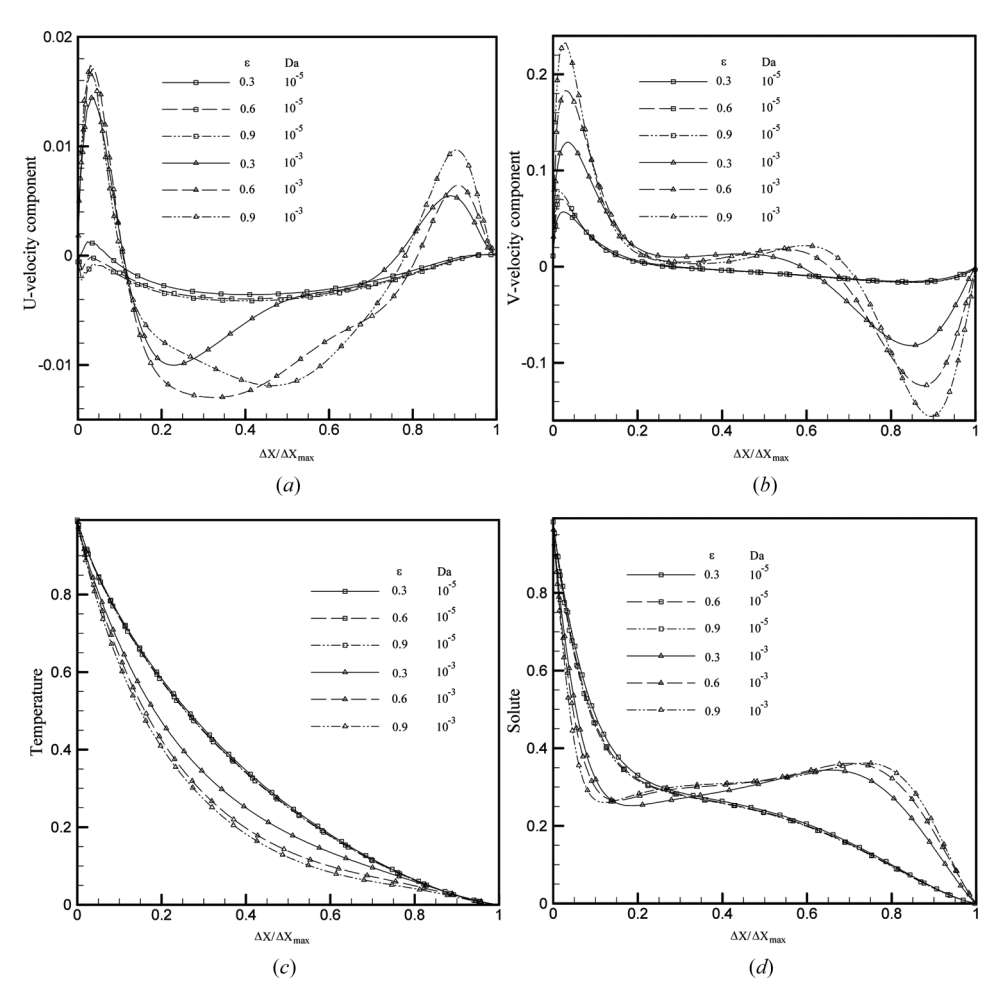


Figure 7. Mid-height (a) U-velocity, (b) V-velocity, (c) temperature, and (d) concentration profiles $(Ra = 10^6, E_g = 0.75, Pr = 0.7, N = 10, and Le = 10)$.

Plots reveal the effects of porosity at two different values of Darcy number for a Rayleigh number of value 10^6 in an enclosure with $E_g = 0.75$ and Pr = 0.7. All profiles indicate that at $Da = 10^{-5}$ porosity has negligible effect on the velocity, temperature, and concentration fields. Moreover, at this value of Darcy number, the values for U and V velocity components (Figures 7a and 7b) are very low indicating negligible convection effects and conduction dominated transfer phenomena with porosity having negligible effect on the velocity profiles except for a small region close to the hot wall. This is further revealed by the temperature and concentration plots depicted in Figures 7c and 7d with profiles at different values of porosity falling nearly on top of each other.

At the higher value of Da (Da = 10^{-3}), the effect of porosity on the velocity (Figures 7a and 7b), temperature (Figure 7c), and concentration (Figure 7d) distribution is obvious. Profiles clearly show the boundary layer behavior close to the hot and cold walls with larger gradients at higher value of ε . The V-velocity profiles (Figure 7b) indicate that the fluid is moving up the hot wall and down the cold wall as reflected by the positive and negatives V-velocity values, respectively. On the other hand, the *U*-velocity values (Figure 7a) are positive along both the hot and cold walls. This is physically correct, and is the result of the positive and negative slopes of the hot and cold wall, respectively. The effect of Da and ε on the temperature and concentration profiles can be easily inferred from the plots presented in Figures 7c and 7d, respectively. The increase in convection contribution to total heat transfer at the higher value of Da is reflected by the nonlinear temperature distribution with convection being higher at higher ε values (increase in nonlinearity of the temperature profile) due to the overall reduction in damping resistance offered by the porous matrix. Similar conclusions can be drawn for variation in concentration with convection effects being more pronounced due to the higher value of Lewis number (Le = 10).

Nusselt and sherwood numbers

The local Nusselt and Sherwood numbers along the inner and outer walls of the porous rhombic annulus are calculated as follows.

$$\begin{aligned}
\mathbf{N}\mathbf{u}_{i/o} &= h_{c,i/o} D_{i/o} / k \ h_{c,i/o} = -k \frac{\nabla T_{i/o} \cdot \mathbf{n}}{T_h - T_c} \\
\mathbf{S}\mathbf{h}_{i/o} &= h_{m,i/o} D_{i/o} / D \ h_{m,i/o} = -D \frac{\nabla S_{i/o} \cdot \mathbf{n}}{S_h - S_c}
\end{aligned}
\Rightarrow \begin{cases}
\mathbf{N}\mathbf{u}_i &= -\frac{D_i}{D_o} \nabla \theta_i \cdot \mathbf{n} \ \mathbf{N}\mathbf{u}_o = -\nabla \theta_o \cdot \mathbf{n} \\
\mathbf{S}\mathbf{h}_i &= -\frac{D_i}{D_o} \nabla S_i \cdot \mathbf{n} \ \mathbf{S}\mathbf{h}_o = -\nabla S_o \cdot \mathbf{n}
\end{aligned}$$
(16)

Furthermore, the average Nusselt and Sherwood number values are defined as follows.

$$\bar{\boldsymbol{h}}_{c,i/o} = \frac{\int\limits_{i/o}^{\int} \left(-k\nabla T_{i/o}\cdot\mathbf{n}\right)ds}{A_{i/o}(T_h - T_c)} \text{ with } \int\limits_{i}^{\int} \left(-k\nabla T_i\cdot\mathbf{n}\right)ds = \int\limits_{o}^{\int} \left(-k\nabla T_o\cdot\mathbf{n}\right)ds \\
\bar{\boldsymbol{h}}_{m,i/o} = \frac{\int\limits_{i/o}^{\int} \left(-D\nabla S_{i/o}\cdot\mathbf{n}\right)ds}{A_{i/o}(T_h - T_c)} \text{ with } \int\limits_{i}^{\int} \left(-D\nabla S_i\cdot\mathbf{n}\right)ds = \int\limits_{o}^{\int} \left(-D\nabla S_o\cdot\mathbf{n}\right)ds \\
\bar{\boldsymbol{N}}_{i/o} = \frac{1}{A_{i/o}}\int\limits_{i/o}^{\int} \boldsymbol{N}\boldsymbol{u}_{i/o}ds \qquad \overline{\boldsymbol{Sh}}_{i/o} = \frac{1}{A_{i/o}}\int\limits_{i/o}^{\int} \boldsymbol{Sh}_{i/o}ds \\
A_i = \frac{D_i}{\cos\Omega}A_o = \frac{D_o}{\cos\Omega}$$

$$(17)$$

Therefore, there is no need to give separate attention to inner and outer Nusselt and Sherwood numbers, and attention will subsequently be focused on $\overline{\text{Nu}}$ and $\overline{\text{Sh}}$. The local Nusselt number distributions along the hot and cold walls are presented in Figures 8a and 8b, respectively, while the corresponding local Sherwood number profiles are displayed in Figures 8c and 8d, respectively. Predictions are presented for two values of Darcy number at $\text{Ra} = 10^6$ in an enclosure with $E_g = 0.75$ and Pr = 0.7. Estimates are plotted as a function of a dimensionless distance $(\Delta Y/\Delta Y_{max})$, defined as follows.

$$\frac{\Delta Y}{\Delta Y_{max}} = \frac{Y - Y_{min}}{Y_{max} - Y_{min}} \tag{18}$$

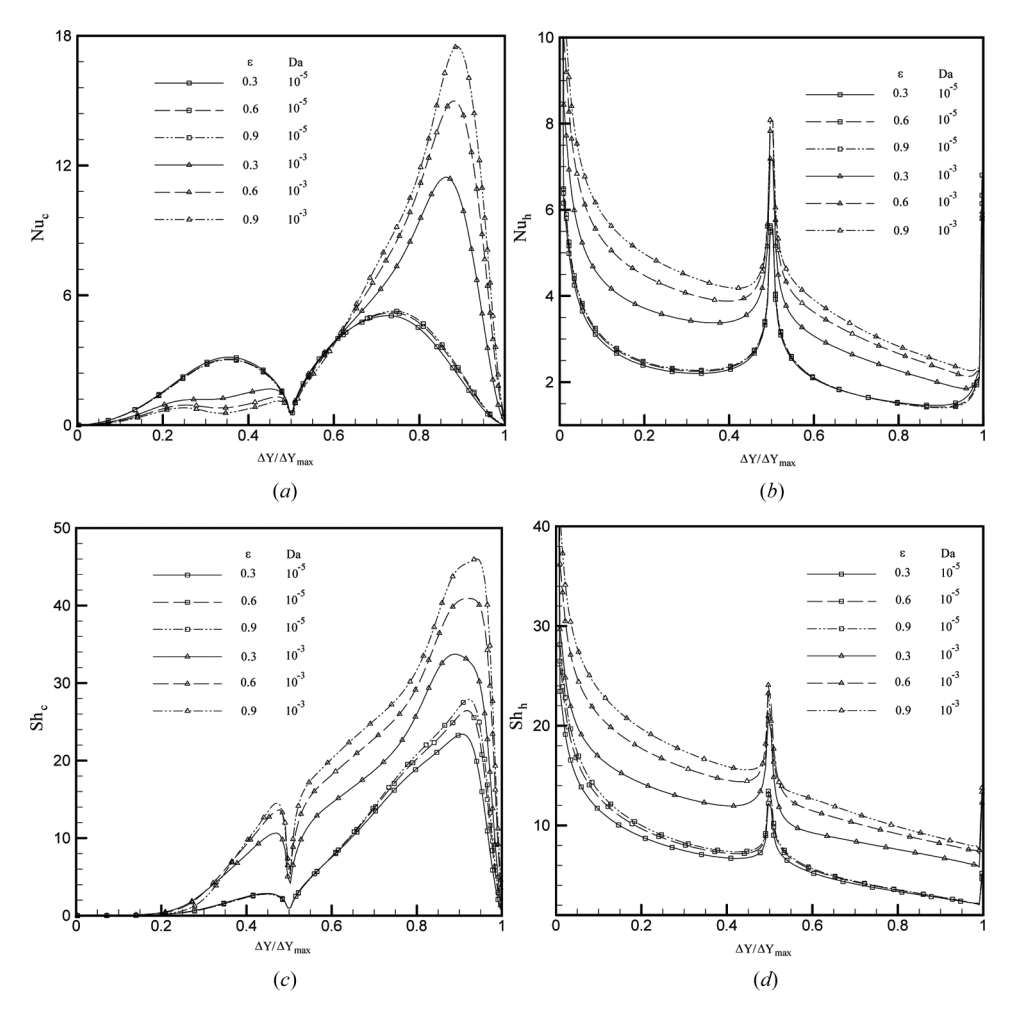


Figure 8. (a),(b) Local Nusselt and (c),(d) Sherwood number distribution along the (a),(c) cold and (b),(d) hot walls of the enclosure (Ra = 10^6 , $E_g = 0.75$, Pr = 0.7, N = 10, and Le = 10).

Nusselt and Sherwood number profiles are similar in shape with Sh values being higher, reflecting the stronger effects of mass transfer over heat transfer (Le = 10). Along the cold/low concentration wall, profiles exhibit two peaks (Figures 8a and 8c), one in the lower half of the enclosure ($\Delta Y/\Delta Y_{max} < 0.5$), and the other in the upper half $(\Delta Y/\Delta Y_{max} > 0.5)$, while passing through a sharp minimum at the middle of the wall ($\Delta Y/\Delta Y_{max} = 0.5$). The local maximum along the lower part is due to the impingement and deflection of the downward descending fluid by the lower portion of the cold/low concentration wall. The upper maximum is due to the hot/high concentration fluid from the inner wall rising upward and impinging on the upper part of the cold/low concentration wall. The sharp minimum at the corner of the outer cold/low concentration wall is due to the tendency of the fluid not to follow the corner contour with a consequent decrease in velocity, heat, and mass transfer. On the other hand, the Nusselt and Sherwood numbers along the hot/high concentration wall peak near the bottom region $(\Delta Y/\Delta Y_{max} = 0)$ and at the middle of the domain $(\Delta Y/\Delta Y_{max} = 0.5)$, with the latter being sharp. The cooled/low concentration fluid from the cold/low concentration wall is transported by the clockwise eddy toward the lower regions of the hot/high concentration wall, and the largest temperature/concentration gradients and Nusselt/Sherwood numbers therefore occur in the leading region of the hot/high concentration wall, thereby maximizing Nu/Sh there. The sharp peak at $\Delta Y/\Delta Y_{max} = 0.5$ is due to the acceleration of the flow until reaching the tip of the lower part of the hot/high concentration wall where it has to change direction to turn around the corner. Beyond that point and because of the increase in temperature/concentration of the fluid in the lower part of the hot/high concentration wall, the rate of heat/mass transfer starts to decrease (i.e., decreasing Nu/Sh), while the fluid temperature/concentration ration continues to increase.

The effects of Darcy number on the variations of local Nusselt and Sherwood numbers along the enclosure walls can be inferred from the two sets of profiles displayed in the various plots (Figures 8a-8d). At low Da value (Da = 10^{-5}), the Nusselt number profiles along the lower and upper parts of the hot and cold walls are similar in shape (Figures 8a and 8b). Along the cold wall, the local maximum of Nusselt number in the lower region is less than that along the upper region because the upward impinging fluid on the upper cold wall is hotter. Along the hot wall the opposite occurs with Nusselt number being higher in the lower portion due to the impingement of the colder fluid there. At high Da, the lower portion becomes increasingly thermally stratified, the downward descending flow penetrates the lower region to a lesser degree, and the maximum Nu in the lower region correspondingly decreases. At high Da, the strength of the convective flow increases in the upper portion of the enclosure as a result of the higher permeability, and consequently, the Nu peak increases along the upper cold wall. Thus, as Da increases, most of the heat transfer along the outer cold wall occurs along its upper portion. Along the inner hot wall, the peaks near the bottom region and at the middle of the domain increase with increasing Da values because of the stronger convective flow as demonstrated by the streamlines and isotherms presented earlier.

Whereas porosity has little effects on Nu profiles at low Da, the level of Nusselt number increases with increasing value of ϵ at high Da due to an increase in the available convective area, leading to a lower hydrodynamic resistance.

Table 2. Average Nusselt number values $\overline{\text{Nu}}$ (N = 10, Le = 10)

	Eg = 0.875, Pr = 0.7							Eg = 0.875, Pr = 5.0						
]	$Da = 10^{-}$	-5	$Da = 10^{-3}$			$Da = 10^{-5}$			$Da = 10^{-3}$				
Ra\ε	0.3	0.6	0.9	0.3	0.6	0.9	0.3	0.6	0.9	0.3	0.6	0.9		
10^{5}	1.46	1.46	1.46	1.68	1.82	1.91	1.46	1.46	1.46	1.72	1.87	1.96		
10^{6}	1.62	1.65	1.66	2.37	2.96	3.22	1.63	1.66	1.67	2.7	3.26	3.5		
10^{7}	2.7	3.14	3.2	4.07	5.53	6.34	3.06	3.32	3.32	4.73	6.08	6.42		
	Eg = 0.75, Pr = 0.7						Eg = 0.75, Pr = 5.0							
]	$Da = 10^{-5}$			$Da = 10^{-3}$			$Da = 10^{-5}$			$Da = 10^{-3}$			
Ra\ε	0.3	0.6	0.9	0.3	0.6	0.9	0.3	0.6	0.9	0.3	0.6	0.9		
10^{5}	2.28	2.29	2.29	2.52	2.7	2.82	2.28	2.29	2.29	2.56	2.75	2.87		
10^{6}	2.46	2.49	2.51	3.52	4.13	4.47	2.48	2.5	2.51	4.04	4.49	4.8		
10^{7}	3.77	4.25	4.36	5.94	7.47	8.53	4.16	4.45	4.5	6.81	8.2	9.24		
	Eg = 0.5, Pr = 0.7						Eg = 0.5, Pr = 5.0							
	$Da = 10^{-5}$			$Da = 10^{-3}$			$Da = 10^{-5}$			$Da = 10^{-3}$				
Ra\ε	0.3	0.6	0.9	0.3	0.6	0.9	0.3	0.6	0.9	0.3	0.6	0.9		
10 ⁵	4.99	4.99	4.99	5.07	5.17	5.27	4.99	4.99	4.99	5.08	5.19	5.29		
10^{6}	5.08	5.1	5.11	5.92	6.56	6.92	5.09	5.11	5.11	6.1	6.78	7.14		
10^{7}	6.2	6.56	6.74	8.41	9.94	11.03	6.52	6.79	6.88	9.27	11.02	12.38		

The variations in Sherwood number (Figures 8c and 8d) are very similar to variations in Nusselt number, except that the values are higher because of the high value of Lewis number considered in the study (Le = 10).

The average Nu and Sh values for all cases studied are given in Tables 2 and 3, respectively, for the two values of Prandtl number for which computations were performed (i.e., Pr = 0.7 and 5). At the lowest Ra considered, the overall heat and mass transfer $\lceil (\overline{Nu}) \text{ and } (\overline{Sh}) \rceil$ appear to be strongly dominated by conduction with convection effects becoming increasingly important on the overall heat and mass transfer as Ra increases. As shown in Tables 2 and 3, at low Ra, convection effects are weak, and although the velocity, temperature, concentration, and heat and mass transfer profiles show mild distortion due to the convective flow (Figures 3-6), these effects are not strong enough to substantially change the overall heat and mass transfer. The larger heat and mass transfer predictions at lower enclosure gap values is due to an increased diffusion contribution as a result of smaller gap width for the same temperature and concentration difference. At Pr = 5 (Tables 2 and 3), the predicted $\overline{\text{Nu}}$ and $\overline{\text{Sh}}$ values are equal to those obtained for Pr = 0.7 at low Ra due to diffusion dominance. As Ra increases, higher Nu and Sh values are obtained at higher Pr indicating greater heat and mass transfer rates. This increase in heat and mass transfer is due to a decrease in the thermal and concentration boundary layer thicknesses, which result in sharper temperature and concentration gradients. The highest $\overline{\text{Nu}}$ and $\overline{\text{Sh}}$ values of 12.38 and 44.09, respectively, are found for the lowest

	<u> </u>							<u> </u>						
	Eg = 0.875, Pr = 0.7							Eg = 0.875, Pr = 5.0						
	$Da = 10^{-5}$			$Da = 10^{-3}$			$Da = 10^{-5}$			$Da = 10^{-3}$				
Ra\ε	0.3	0.6	0.9	0.3	0.6	0.9	0.3	0.6	0.9	0.3	0.6	0.9		
10 ⁵	1.84	1.87	1.89	4.51	5.39	5.93	1.84	1.87	1.89	4.64	5.50	6.07		
10^{6}	5.36	5.85	6.09	8.06	10.37	11.11	5.51	5.93	6.14	8.43	10.67	11.37		
10^{7}	12.22	15.11	15.65	14.81	20.05	22.79	13.83	15.85	16.19	15.76	20.83	21.67		
		Eg = 0.75, Pr = 0.7						Eg = 0.75, Pr = 5.0						
		$Da = 10^{-5}$			$Da = 10^{-3}$			$Da = 10^{-5}$			$Da = 10^{-3}$			
Ra\ε	0.3	0.6	0.9	0.3	0.6	0.9	0.3	0.6	0.9	0.3	0.6	0.9		
10 ⁵	2.63	2.66	2.68	6.47	7.77	8.59	2.63	2.67	2.68	6.64	7.91	8.71		
10^{6}	7.19	7.79	8.05	12.08	14.76	16.11	7.41	7.9	8.13	13.78	15.22	16.44		
10^{7}	16.97	20.36	21.44	22.8	28.21	32.11	18.93	21.43	22.25	24.04	29.24	33.28		
	Eg = 0.5, Pr = 0.7						Eg = 0.5, Pr = 5.0							
	$Da = 10^{-5}$			$Da = 10^{-3}$			$Da = 10^{-5}$			$Da = 10^{-3}$				
Ra\ε	0.3	0.6	0.9	0.3	0.6	0.9	0.3	0.6	0.9	0.3	0.6	0.9		
105	5.12	5.14	5.15	8.42	10.55	11.85	5.12	5.14	5.15	8.63	10.77	12.04		
10^{6}	9.08	9.73	10.02	16.74	20.47	22.5	9.34	9.86	10.1	17.36	20.98	22.97		
10^{7}	22.55	26.11	27.97	31.2	38.29	43.09	24.83	27.77	29.06	32.61	39.32	44.09		

Table 3. Average Sherwood number values \overline{Sh} (N = 10, Le = 10)

 E_g and the highest Da, Ra, Pr, and ε . While the lowest $\overline{\text{Nu}}$ and $\overline{\text{Sh}}$ of 1.46 and 1.84, respectively, are attained at the highest E_g and the lowest Da, Ra, Pr, and ε . Furthermore, when conduction is the dominant heat transfer mode predicted $\overline{\text{Nu}}$ and $\overline{\text{Sh}}$ values depend only on E_g .

CONCLUSION

This article investigated numerically, using a finite volume method, double diffusive natural convection in a porous enclosure of rhombic cross-section. Simulations examined, at fixed values of Lewis number and buoyancy ratio, the effects of Raleigh number, Darcy number, porosity, enclosure gap, and Prandtl number on natural convection within the enclosure. Results indicated that convection effects increase with an increase in Ra, Da, E_g , and/or ϵ . Predictions also revealed that porosity has no effect on the flow, temperature, and concentration fields at low values of Da. The total heat and mass transfer rates were found to be higher at higher Pr values and to be diffusion-dominated at low Ra, with contribution due to convection increasing at high Ra values.

REFERENCES

 T. Nishimura, T. Imoto, and H. Miyashita, Occurrence and Development of Double Diffusive Convection during Solidification of a Binary System, *Int. J. of Heat and Mass Transfer*, vol. 37, pp. 1455–1464, 1994.

- 2. B. I. Makham and F. Rosenberger, Diffusive Convection Vapor Transport Across Horizontal and Inclined Rectangular Enclosures, *J. of Crystal Growth*, vol. 67, pp. 241–254, 1984.
- 3. T. L. Bergman, F. P. Incropera, and R. Viskanta, Correlation of Mixed Layer Growth in a Double Diffusive, Salt-Stratified System Heated from Below, *J. of Heat Transfer*, vol. 108, pp. 206–211, 1986.
- 4. J.-O. Carlsson, Processes in Interfacial Zones During Chemical Vapor Deposition: Aspects of Kinetics, Mechanisms, Adhesion and Substrate Atom Transport, *Thin Solid Films*, vol. 130, pp. 261–282, 1985.
- 5. Y. Varol, H. F. Oztop, and I. Pop, Numerical Analysis of Natural Convection for a Porous Rectangular Enclosure with Sinusoidally Varying Temperature Profile on the Bottom Wall, *Int. Commu. Heat and Mass Transfer*, vol. 35, pp. 56–64, 2008.
- 6. G. B. Kim, J. M. Hyun, and H. S. Kwak, Buoyant Convection in a Square Cavity Partially Filled with a Heat-Generating Porous Medium, *Numer. Heat Transfer A*, vol. 40, pp. 601–618, 2001.
- 7. M. A. Hossain and M. Wilson, Natural Convection Flow in a Fluid-Saturated Porous Medium Enclosed by Non-Isothermal Walls with Heat Generation, *Int. J. of Therm. Sci.*, vol. 41, pp. 447–454, 2002.
- 8. S. Das, and R. K. Sahoo, Effect of Darcy, Fluid Rayleigh and Heat Generation Parameters on Natural Convection in a Porous Square Enclosure: A Brinkman-Extended Darcy Model, *Inte. Comm. in Heat and Mass Transfer*, vol. 26, no. 4, pp. 569–578, 1999.
- 9. T. Basak, S. Roy, A. Singh, and A. R. Balakrishnan, Natural Convection Flows in Porous Trapezoidal Enclosures with Various Inclination Angles, *Int. J. of Heat and Mass Transfer*, vol. 52, pp. 4612–4623, 2009.
- T. Basak, S. Roy, S. K. Babu, and I. Pop, Finite Element Simulations of Natural Convection Flow in an Isosceles Triangular Enclosure Filled with a Porous Medium: Effects of Various Thermal Boundary Conditions, *Int. J. of Heat and Mass Transfer*, vol. 51, pp. 2733–2741, 2008.
- 11. X. B. Chen, P. Yu, S. H. Winoto, and H. T. Low, Free Convection in a Porous Wavy Cavity Based on the Darcy–Brinkman–Forchheimer Extended Model, *Numer. Heat Transfer A*, vol. 52, pp. 377–397, 2007.
- 12. F. Moukalled and M. Darwish, Natural Convection Heat Transfer in a Porous Rhombic Annulus, *Nume. Heat Transfer A*, vol. 58, no. 1, pp. 101–124, 2010.
- 13. J. Lee, M. T. Hyun, and J. H. Moh, Numerical Experiments on Natural Convection in a Stably Stratified Fluid due to Side-Wall Heating, *Numer. Heat Transfer A*, vol. 18, no. 3, pp. 343–355, 1990.
- 14. J. W. Lee and J. M. Hyun, Double Diffusive Convection in a Rectangle with Opposing Horizontal Temperature and Concentration Gradients, *Int. J. of Heat and Mass Transfer*, vol. 33, no. 8, pp. 1619–1632, 1990.
- M. N. Borjini, L. Kolsi, N. Daous, and H. Ben Aissia, Hydromagnetic Double Diffusive Laminar Natural Convection in a Radiatively Participating Fluid, *Numer. Heat Transfer A*, vol. 48, no. 5, pp. 483–506, 2005.
- M. N. Borjini, H. Ben Aissia, K. Halouani, and B. Zeghmati, Effect of Optical Properties on Oscillatory Hydromagnetic Double Diffusive Convection within Semitransparent Fluid, *Int. J. of Heat and Mass Transfer*, vol. 49, nos. 21–22, pp. 3984–3996, 2006.
- 17. H. Han and T. H. Kuehn, Double Diffusive Natural Convection in a Vertical Rectangular Enclosure—II. Numerical Study, *Int. J. of Heat and Mass Transfer*, vol. 34, no. 2, pp. 461–471, 1991.
- 18. S. Y. Wang, C. X Lin, and M. A Ebadian, Study of Double Diffusive Velocity during the Solidification Process using Particle Image Velocimetry, *Int. J. of Heat and Mass Transfer*, vol. 42, no. 24, pp. 4427–4445, 1999.

- 19. K. Shi and W.-Q. Lu, Time Evolution of Double Diffusive Convection in a Vertical Cylinder with Radial Temperature and Axial Solutal Gradients, *Int. J. of Heat and Mass Transfer*, vol. 49, nos. 5–6, pp. 995–1003, 2006.
- 20. J. Lee, S. H. Kang, and Y. S. Son, Experimental Study of Double Diffusive Convection in a Rotating Annulus with Lateral Heating, *Int. J. of Heat and Mass Transfer*, vol. 42, no. 5, pp. 821–832, 1999.
- 21. J. Doschan, H. Beer, Numerical Simulation and Holographic Visualization of Double Diffusive Convection in a Horizontal Concentric Annulus, *Int. J. of Heat and Mass Transfer*, vol. 35, no. 7, pp. 1811–1821, 1992.
- 22. J. Liou and Z. Hong, Numerical Simulation of Double Diffusive Natural Convection in a V-Shaped Sump by a Control Volume Method Based on Unstructured Triangular Grid, *Numer. Heat Transfer A*, vol. 34, no. 4, pp. 431–446, 1998.
- 23. D. S. Kumar, K. Murugesan, and H. R. Thomas, Numerical Simulation of Double Diffusive Mixed Convection in a Lid-Driven Square Cavity using Velocity-Vorticity Formulation, *Numer. Heat Transfer A*, vol. 54, no. 9, pp. 837–865, 2008.
- 24. D. S. Kumar, K. Murugesan, and H. R. Thomas, Effect of the Aspect Ratio of a Heated Block on the Interaction Between Inertial and Thermosolutal Buoyancy Forces in a Lid-Driven Cavity, *Numer. Heat Transfer A*, vol. 60, no. 7, pp. 604–628, 2011.
- 25. F. Suárez, S. W. Tyler, and A. E. Childress, A Fully Coupled, Transient Double Diffusive Convective Model for Salt-Gradient Solar Ponds, *Int. J. of Heat and Mass Transfer*, vol. 53, nos. 9–10, pp. 1718–1730, 2010.
- E. J. Kranenborg and H. A. Dijkstra, Double Diffusive Layer Formation Near a Cooled Liquid-Solid Boundary, *Int. J. of Heat and Mass Transfer*, vol. 41, no. 13, pp. 1873–1884, 1998.
- 27. H. A. Dijkstra, and E. J. Kranenborg, A Bifurcation Study of Double Diffusive Flows in a Laterally Heated Stably Stratified Liquid Layer, *Int. J. of Heat and Mass Transfer*, vol. 39, no. 13, pp. 2699–2710, 1996.
- 28. J. Tanny and V. A. Gotlib, Linear Stability of a Double Diffusive Layer with Variable Fluid Properties, *Int. J. of Heat and Mass Transfer*, vol. 38, no. 9, pp. 1683–1691, 1995.
- 29. E. J. Kranenborg and H. A. Dijkstra, On the Evolution of Double Diffusive Intrusions into a Stably Stratified Liquid: A Study of the Layer Merging Process, *Int. J. of Heat and Mass Transfer*, vol. 41, no. 18, pp. 2743–2756, 1998.
- 30. J. T. Van Der Eyden, T. H. Van Der Meer, K. Hanjalić, E. Biezen, and J. Bruining, Double Diffusive Natural Convection in Trapezoidal Enclosures, *Int. J. of Heat and Mass Transfer*, vol. 41, no. 13, pp. 1885–1898, 1998.
- 31. T. A. Hullender and W. R. Laster, Numerical Model of Wind-Induced Entrainment in a Double Diffusive Thermohaline System, *Numer. Heat Transfer A*, vol. 25, no. 1, pp. 43–55, 1994.
- 32. M. J. S. de Lemos and L. A. Tofaneli, Modeling of Double Diffusive Turbulent Natural Convection in Porous Media, *Int. J. of Heat and Mass Transfer*, vol. 47, no. 19–20, pp. 4233–4241, 2004.
- 33. M. Karimi-Fard, M. C. Charrier-Mojtabi, and K. Vafai, Non-Darcian Effects on Double Diffusive Convection within a Porous Medium, *Numer. Heat Transfer A*, vol. 31, no. 8, pp. 837–852, 1997.
- 34. A. J. Chamkha, Double Diffusive Convection in a Porous Enclosure with Cooperating Temperature and Concentration Gradients and Heat Generation or Absorption Effects, *Numer. Heat Transfer A*, vol. 41, no. 1, pp. 65–87, 2002.
- 35. R. Bennacer, H. Beji, F. Oueslati, and A. Belghith, Multiple Natural Convection Solution in Porous Media under Cross Temperature and Concentration Gradients, *Numer. Heat Transfer A*, vol. 39, no. 6, pp. 553–567, 2001.

- 36. H. Beji, R. Bennacer, R. Duval, and P. Vasseur, Double Diffusive Natural Convection in a Vertical Porous Annulus, *Numer. Heat Transfer A*, vol. 36, no. 2, pp. 153–170, 1999.
- 37. V. A. F. Costa, Double Diffusive Natural Convection in Parallelogrammic Enclosures Filled with Fluid-Saturated Porous Media, *Int. J. of Heat and Mass Transfer*, vol. 47, no. 12–13, pp. 2699–2714, 2004.
- 38. V. A. F. Costa, Double Diffusive Natural Convection in Parallelogrammic Enclosures, *Int. J. of Heat and Mass Transfer*, vol. 47, no. 14–16, pp. 2913–2926, 2004.
- 39. B. V. R. Kumar, P. Singh, and V. J. Bansod, Effect of Thermal Stratification on Double Diffusive Natural Convection in a Vertical Porous Enclosure, *Numer. Heat Transfer A*, vol. 41, no. 4, pp. 421–447, 2002.
- 40. M. Z. Saghir, and M. R. Islam, Double Diffusive Convection in Dual-Permeability, Dual-Porosity Porous Media, *Int. J. of Heat and Mass Transfer*, vol. 42, no. 3, pp. 437–454, 1999
- 41. K. Vafai, and C. L. Tien, Boundary, and Inertia Effects on Flow, and Heat Transfer in Porous Media, *Int. J. of Heat and Mass Transfer*, vol. 24, pp 195–203, 1981.
- 42. H. C. Brinkman, On the Permeability of Media Consisting of Closely Packed Porous Particles, *Appl. Sci. Res.*, vol. 1, pp. 81–86, 1947.
- 43. A. Amiri, and K. Vafai, Analysis of Dispersion Effect, and Non-Thermal Equilibrium, Non-Darcian Variable Porosity Incompressible Flow through Porous Media, *Int. J. of Heat and Mass Transfer*, vol. 37, pp. 939–954, 1994.
- 44. P. J. Zwart, G. D. Raithby, and M. J. Raw, An Integrated Space-Time Finite-Volume Method for Moving-Boundary Problems, *Numer. Heat Transfer B*, vol. 34, pp. 257–270, 1998.
- 45. P. H. Gaskell and A. K. C. Lau, Curvature Compensated Convective Transport: SMART, A New Boundedness Preserving Transport Algorithm, *Int. J. for Numer. Methods in Fluids*, vol. 8, pp. 617–641, 1988.
- 46. M. Darwish and F. Moukalled, Normalized Variable and Space Formulation Methodology for High-Resolution Schemes, *Numer. Heat Transfer B*, vol. 26, pp. 79–96, 1994.
- 47. S. V. Patankar, *Numerical Heat Transfer and Fluid Flow*, Hemisphere Publishing Corporation, New York, 1980.
- 48. F. Moukalled, and M. Darwish, Pressure Based Algorithms for Single, and Multifluid Flow, in W. J. Minkowycz, E. M. Sparrow, and J. Y. Murthy (eds.), *Handbook of Numerical Heat Transfer*, 2nd ed., pp. 325–367, Wiley, New Jersey, 2006.
- 49. F. Moukalled and M. Darwish, A Unified Formulation of the Segregated Class of Algorithms for Fluid Flow at All Speeds, *Numer. Heat Transfer B*, vol. 37, no. 1, pp. 103–139, 2000
- M. Peric, A Finite Volume Method for the Prediction of Three-Dimensional Fluid Flow in Complex Ducts, Ph.D. Thesis, Imperial College, Mechanical Engineering Department, London, UK, 1985.
- 51. B. Goyeau, J.-P. Songbe, and D. Gobin, Numerical Study of Double Diffusive Natural Convection in Porous Cavity using the Darcy-Brinkman Formulation, *Int. J. of Heat and Mass Transfer*, vol. 39, pp. 1363–1378, 1996.
- 52. O. V. Trevisan and A. Bejan, Natural Convection with Combined Heat and Mass Transfer Buoyancy Effects in a Porous Medium, *Int. J. of Heat and Mass Transfer*, vol. 28, pp. 1597–1611, 1985.